Multistatic 3-D microwave imaging with dynamic metasurface antennas: a Fourier-based approach

Amir Masoud Molaei*[a], Thomas Fromenteze[b], Vasiliki Skouroliakou[a], Shaoqing Hu[c], Vincent Fusco[a], Okan Yurduseven[a]

[a]Centre for Wireless Innovation (CWI), Queen's University Belfast, Queen's Road, Belfast, U.K. BT3 9DT; [b]Xlim Research Institute, University of Limoges, Limoges, France 87060; [c]College of Engineering, Design and Physical Sciences, Brunel University London, Kingston Lane, Uxbridge, U.K. UB8 3PH

ABSTRACT

This paper proposes a novel approach to 3-D microwave imaging using dynamic metasurface antennas in a multistatic configuration. By introducing a panel-to-panel model and a preprocessing technique, raw measurements are converted into the space-frequency domain for efficient data acquisition and reconstruction. Adapting the range migration algorithm in this work enables fast Fourier-based image reconstruction. Simulation results showcase the effectiveness of the proposed method, highlighting its potential for real-world applications.

Keywords: Adapted range migration algorithm, dynamic metasurface antennas, near-field multistatic microwave imaging, 3-D image reconstruction

1. INTRODUCTION

Microwave imaging plays a crucial role in various applications such as biomedical diagnostics, concealed weapon detection and nondestructive testing [1-5]. Traditional imaging systems often rely on mechanical or electronic raster scans (by sequentially switched arrays), which can be slow and power-hungry [6]. Dynamic metasurface antennas (DMAs) [7] offer a promising alternative due to their small form-factor, reduced power consumption, and ease of fabrication [8, 9]. However, the unique radiation patterns of DMAs pose challenges for fast Fourier-based image reconstruction algorithms [10, 11] due to physical layer compression [12]. An effective solution for this issue, using sub-wavelength sampling of the aperture, is detailed in [13-16], which outlines how measurements can be expressed in the spatial domain. These studies employ a panel-to-probe model, utilizing a single 1-D DMA on the transmitter (TX) side and a rectangular waveguide probe (point source) on the receiver (RX) side. In this configuration, either the TX DMA or the RX must physically move to create a large effective aperture and capture 2-D/3-D images of the scene from the collected data. However, this approach lowers data acquisition rates and is not suitable for real-time applications.

Although the approach presented in [17] provides a panel-to-panel model with full electronic scanning, it is limited to a bistatic structure. In this paper, we introduce a panel-to-panel model by employing DMAs in a more general imaging structure (i.e. multistatic) to address the challenges mentioned above. We present a preprocessing technique to convert raw measurements into the space-frequency domain, enabling efficient data acquisition and reconstruction. By adapting the range migration algorithm (RMA) to the imaging system configuration, we achieve 3-D image reconstructions with fast Fourier calculations. Key contributions include introducing a panel-to-panel model in a multistatic structure, presenting a preprocessing technique with data collected from all channels, and deriving a mathematical solution for scene image reconstruction based on fast Fourier computations. The effectiveness of the proposed method is investigated and discussed through numerical simulations.

The rest of this paper is organized as follows. Section 2 covers the proposed approach, detailing the system model, preprocessing procedure and 3-D image reconstruction algorithm. Section 3 presents and discusses the simulation results. Finally, Section 4 offers the conclusion.

*a.molaei@qub.ac.uk; fax 44 28 9097 1702; pure.qub.ac.uk/en/persons/amir-masoud-molaei

Notation: Throughout the paper, superscripts $(\cdot)^T$ and $(\cdot)^{\dagger}$ represent the transpose and pseudo-inverse, respectively. The symbols j, δ denote the imaginary unit and Dirac delta function, respectively.

2. PROPOSED APPROACH

Figure 1 depicts a general layout of the proposed multistatic imaging system. This system uses N_T DMAs for transmission along the horizontal x-axis and one DMA for reception along the vertical y-axis. Each TX and RX DMA is a 1-D array with N_x and N_y metamaterial elements, respectively, with d_x and d_y inter-element spacing. The metamaterial elements are loaded with reconfigurable structures, such as PIN or varactor diodes, to control their radiation characteristics [18]. The system varies the radiation patterns by adjusting the operating frequency f [19-21] and/or tuning the voltage of the diodes, which randomly activates or deactivates the metamaterial elements to create different masks [22]. Each TX DMA can generate multiple measurements by cycling through M_T masks. Objects in the scene scatter the incident fields, which are then detected by the RX DMA with M_R masks. The number of masks influences the system's diversity and complexity [23].
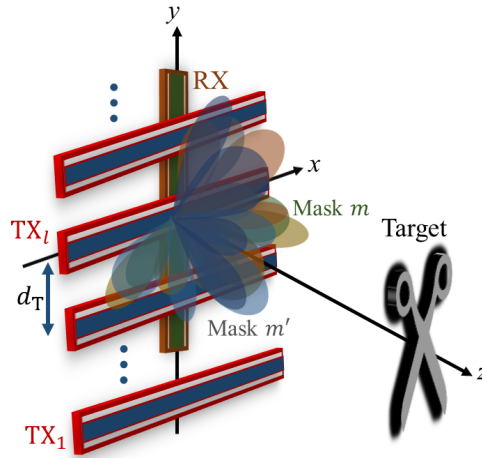

Figure 1. The general layout of the proposed multistatic imaging system.

The measurement signal can be represented as [23]

$$g_{l,m,m'}(f) = \int_V U_m(y_l, \vec{r}, f)\rho(\vec{r})U'_{m'}(\vec{r}, f)dV, \quad l = 1,2,...,N_T, \ m = 1,2,...,M_T, \ m' = 1,2,...,M_R, \tag{1}$$

where $dV = dxdydz$ denotes a small volume element made of space intervals dx, dy and dz in the directions x, y and z, respectively, $y_l = y_1 + ld_T$ is the vertical position of the l-th Tx, ρ is the target reflectivity [24], and $\vec{r}$ is the position vector to a point in the scene. U and U' are the radiated fields from the TX and RX apertures, which are superpositions of the fields from all metamaterial elements, and are calculated by (2) from [23].

The measured signal on the aperture plane, expanded in terms of fields associated with all masks, is [23]

$$g_{l,m,m'}(f) = \sum_{i=1}^{N_x}\sum_{i'=1}^{N_y}\Phi_{l,m}(x_i, f)s_l(x_i, y_{i'}, f)\Phi'_{m'}(y_{i'}, f), \tag{2}$$

where $s_l(x_i, y_{i'}, f)$ represents the incident field at the location of the l-th TX, and x_i and $y_{i'}$ correspond to the positions of TX and RX, respectively. The fields over the aperture corresponding to the masks, $\Phi_{l,m}$ and $\Phi'_{m'}$, are a function of wave impedance in free space, guided magnetic field, polarizability and propagation constant of the waveguide, the details of their calculation are given in [22, 25].

Assuming orthogonal aperture modes [23]

$$\sum_{i=1}^{N_x} \Phi_{l,m}(x_i,f)\Phi_{l,\tilde{m}}^{\dagger}(x_i,f) \simeq \delta[m-\tilde{m}], \quad \tilde{m}\in[1,M_{\mathrm{T}}], \tag{3}$$

$$\sum_{i'=1}^{N_y} \Phi_{\tilde{m}'}'^{\dagger}(y_{i'},f)\Phi_{m'}'(y_{i'},f) \simeq \delta[\tilde{m}'-m'], \quad \tilde{m}'\in[1,M_{\mathrm{R}}]. \tag{4}$$

With dynamic modulation of the aperture using different masks, the measurement signal can be transformed and estimated as [22]

$$s_l(x_i,y_{i'},f) \simeq \sum_{m=1}^{M_{\mathrm{T}}}\sum_{m'=1}^{M_{\mathrm{R}}} \Phi_{l,m}^{\dagger}(x_i,f)\, g_{l,m,m'}(f)\,\Phi_{m'}'^{\dagger}(y_{i'},f). \tag{5}$$

This allows fast Fourier calculations for data processing, expressed in matrix form as [26]

$$\mathbf{s}_l(f) \simeq \mathbf{\Phi}_l^{\dagger}(f)\mathbf{g}_l(f)\left(\mathbf{\Phi}'^{T}(f)\right)^{\dagger}. \tag{6}$$

By using the system geometry and 3-D Fourier transforms, the signal in the wavenumber domain is [23]

$$S\left(k_{x\mathrm{T}},k_{y\mathrm{T}},k_{y\mathrm{R}},k\right) \simeq \frac{K}{16\pi^2}\int_V \rho(x,y,z)\,e^{-jk_{x\mathrm{T}}x}e^{-j(k_{y\mathrm{T}}+k_{y\mathrm{R}})y}e^{-j\sqrt{k^2-k_{x\mathrm{T}}^2-k_{y\mathrm{T}}^2}z}e^{-j\sqrt{k^2-k_{y\mathrm{R}}^2}z}\,dV, \quad k^2\ge k_{y\mathrm{R}}^2,\; k^2\ge k_{x\mathrm{T}}^2+k_{y\mathrm{T}}^2, \tag{7}$$

where $k=2\pi f/c$, c denotes the speed of light, and K is the filtering factor in the Fourier domain [23]. Finally, by performing Stolt interpolation and applying inverse Fourier transforms, the reflectivity $\rho(x,y,z)$ can be recovered [23, 26].

Note that in conventional systems with independent antennas, the field is described by Green's function, while DMAs encode scene information through their random transfer function, eliminating the need for point-by-point sampling but requiring more complex signal descriptions. The preprocessing in (6) transforms DMA measurements into data equivalent to that from traditional antenna arrays.

3. SIMULATION RESULTS AND DISCUSSION

In this section, the performance of the proposed approach is evaluated using numerical simulations conducted in MATLAB. The simulations were carried out on a system running MATLAB R2020b on a 64-bit Windows 11 operating system, equipped with 16 GB of random-access memory and a Core-i7 processor clocked at 2.8 GHz. The data used in the numerical examples were generated using the model described in (1), under the first Born approximation [27]. The simulation parameters are listed in Table 1, where λ denotes the wavelength corresponding to the highest frequency in free space, N_{f} indicates the number of frequency samples, z_0 is the target range.

Table 1. The values of the main simulation parameters.

Parameter	$N_x=N_y$	N_{T}	$d_x=d_y$	d_{T}	$M_{\mathrm{T}}=M_{\mathrm{R}}$	f	N_{f}	z_0
Value	105	3	$\lambda/2$	26λ	105	17.5-22 GHz	51	0.5 m

Before reconstructing the image, it is important to verify the condition outlined in (3) and (4). Figure 2 displays the aperture field matrices $\mathbf{\Phi}_1$, $\mathbf{\Phi}_2$, $\mathbf{\Phi}_3$ and $\mathbf{\Phi}'$ at 22 GHz for a random scenario where half of the elements in each mask are randomly activated. Figures 3(a)-3(d) depict $\mathbf{\Phi}_1\mathbf{\Phi}_1^{\dagger}$, $\mathbf{\Phi}_2\mathbf{\Phi}_2^{\dagger}$, $\mathbf{\Phi}_3\mathbf{\Phi}_3^{\dagger}$ and $\left(\mathbf{\Phi}'^{T}\right)^{\dagger}\mathbf{\Phi}'^{T}$ at 22 GHz, respectively, showing that it satisfies conditions (3) and (4), making it viable for the preprocessing step. In addition, Figures 3(e) and 3(f) show $\mathbf{\Phi}_1\mathbf{\Phi}_2^{\dagger}$ and $\mathbf{\Phi}_1\mathbf{\Phi}_3^{\dagger}$ at 22 GHz, respectively. The non-orthogonality between the aperture field matrices corresponding to different TXs is the key property used in [23] to recover contributions of TXs in a scenario where they transmit simultaneously. Similar analyzes can be performed for other frequencies.
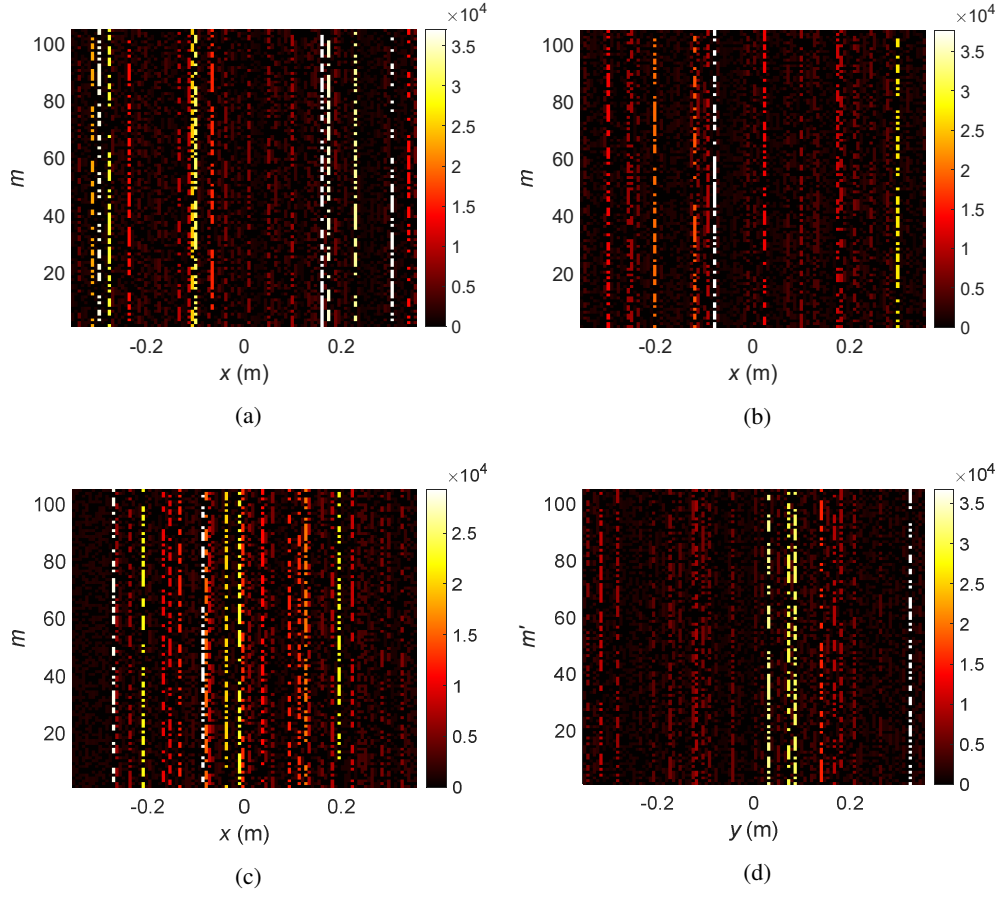
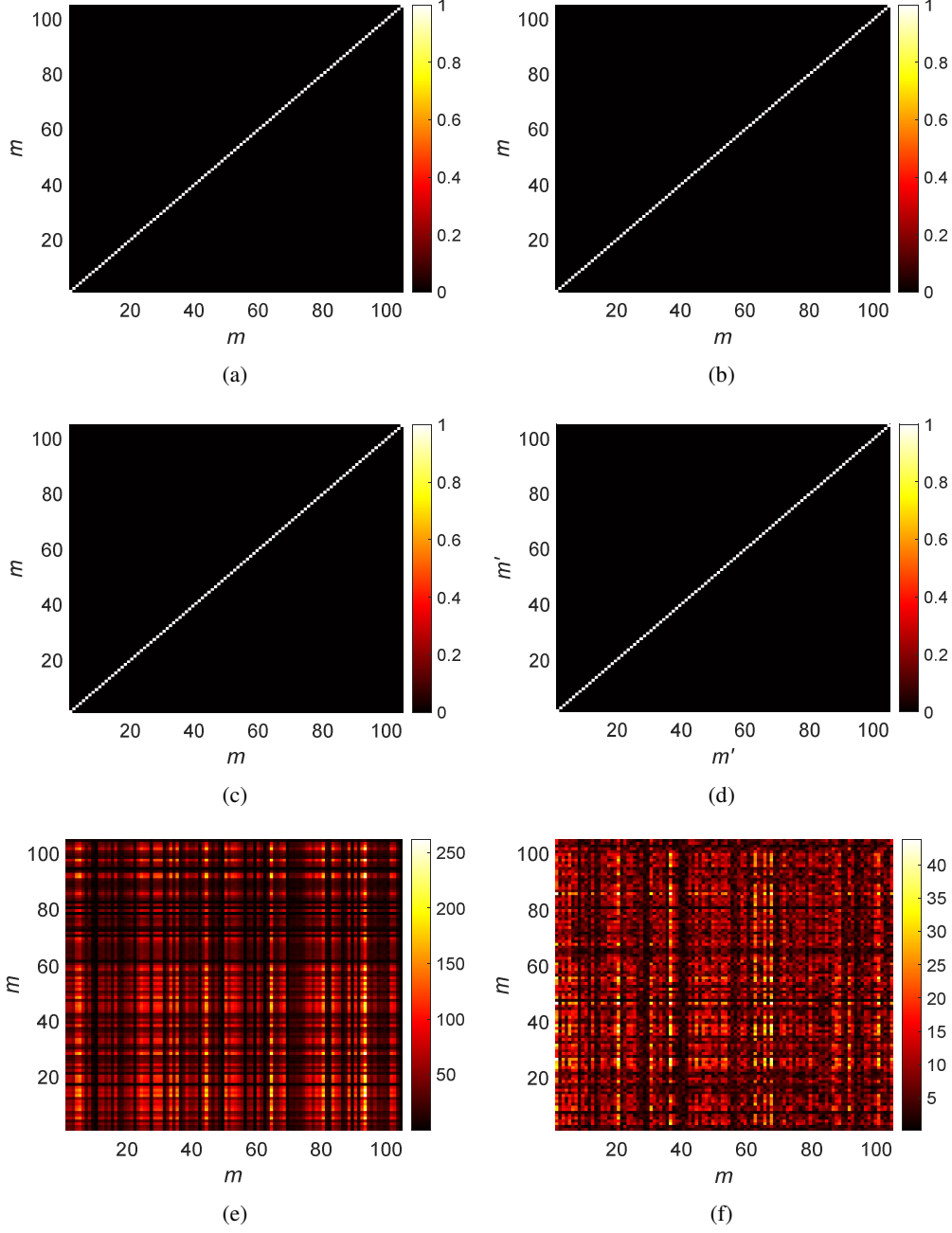Figure 2. The aperture field matrices at 22 GHz for a random scenario; (a) $\mathbf{\Phi}_1$, (b) $\mathbf{\Phi}_2$, (c) $\mathbf{\Phi}_3$, (d) $\mathbf{\Phi}'$.

Figure 3. Checking the orthogonality between the aperture field matrices at 22 GHz; (a) $\mathbf{\Phi}_1\mathbf{\Phi}_1^\dagger$, (b) $\mathbf{\Phi}_2\mathbf{\Phi}_2^\dagger$, (c) $\mathbf{\Phi}_3\mathbf{\Phi}_3^\dagger$, (d) $\left(\mathbf{\Phi'}^T\right)^\dagger\mathbf{\Phi'}^T$, (e) $\mathbf{\Phi}_1\mathbf{\Phi}_2^\dagger$, (f) $\mathbf{\Phi}_1\mathbf{\Phi}_3^\dagger$.

For further study, we calculated the average value of condition number r , which is defined as the ratio of the largest to the smallest singular values of the aperture field, in 1000 independent experiments for different numbers of masks and percentage of active elements (denoted by P). Ideally, the condition number should be 1, suggesting a flat singular value decomposition pattern [28, 29]. This would mean that the orthogonality of the measurement modes is perfect. The results, shown in Figure 4, indicate that as P increases, the value of r also increases, meaning lower percentages of activated metamaterial elements provide more reliable orthogonality conditions [22]. However, fewer activated elements

also result in lower radiated power, leading to a reduced signal-to-noise ratio [22]. Therefore, a moderate P value (with half the elements activated) offers a balanced trade-off between orthogonality and noise robustness.
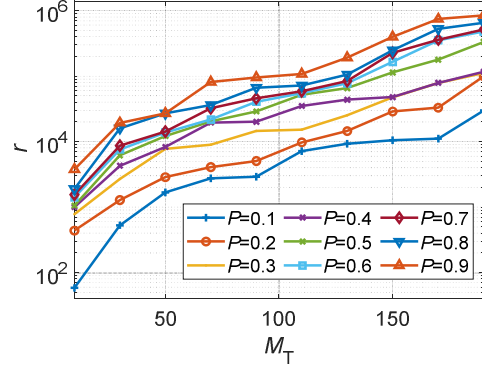

Figure 4. The average value of r in 1000 independent experiments in the case of Φ_1 at 22 GHz.

Now let us examine the performance of the image reconstruction algorithm. A 3-D distributed target (scissors) is considered in the near-field [30] scenario (see Figure 1). Figure 5 shows the successfully reconstructed image of the target using the proposed approach. The total computational time for implementing the image reconstruction algorithm is 13.33 seconds. The main steps of implementing the algorithm, including a preprocessing operation to convert the raw measured data to the spatial-frequency domain, fast Fourier transform (FFT), 4-D to 3-D Stolt interpolation and inverse FFT, take 11.71%, 4.8%, 83.05% and 0.44% of the total computing time, respectively. As can be seen, most of the computational burden is related to the Stolt interpolation step. Note that the computational time of the proposed approach is much less compared to algorithms such as least squares, matched filtering and generalized synthetic aperture focusing technique [31]. For more details on the comparison of computational times and computational complexities, see [23].
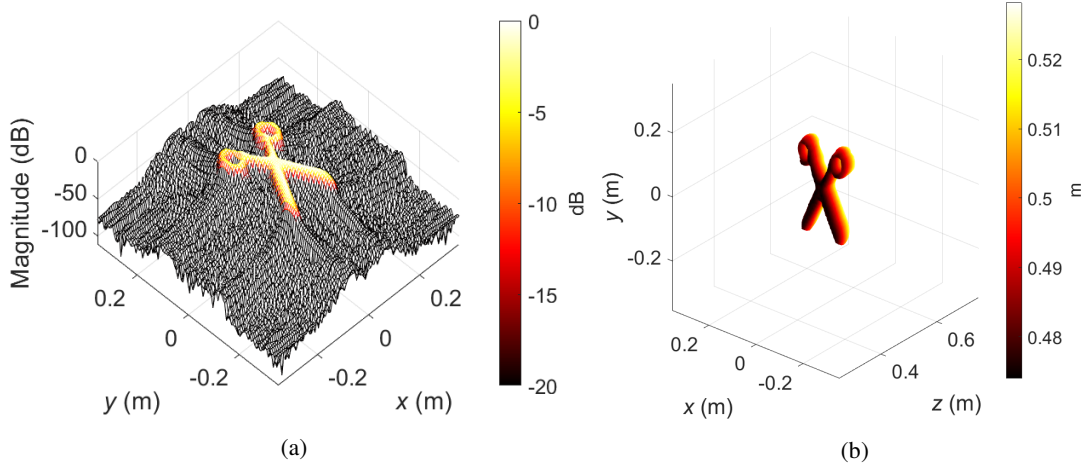

(a)
(b)

Figure 5. The reconstructed image using the proposed approach; (a) mesh surface plot focused on $z_0 = 0.5\,\mathrm{m}$ (colorbar is on the dB scale and represents the normalized reflectivity magnitude), (b) isosurface with 3-D view (colorbar is range-coded, representing the distance).

4. CONCLUSION

In this paper, we presented a novel approach to 3-D microwave imaging utilizing DMAs in a multistatic configuration. Our method introduces a panel-to-panel model that significantly improves data acquisition efficiency and enables fast Fourier-based image reconstruction. By employing a preprocessing technique to convert raw measurements into the space-frequency domain and adapting the RMA for this configuration, we demonstrated an effective 3-D image reconstruction. The simulation results validated the proposed method's efficacy, showing that it achieves accurate imaging with low computational time. This approach opens new avenues for real-time, high-resolution imaging in

various applications, including security screening and biomedical diagnostics. Future work will focus on further optimizing the system for real-world deployment.

ACKNOWLEDGMENT

REFERENCES

[1] K. Lalitha and J. Manjula, "Non-invasive microwave head imaging to detect tumors and to estimate their size and location," *Physics in Medicine,* vol. 13, p. 100047, 2022.

[2] A. O. Asok, G. N. SJ, and S. Dey, "Microwave imaging with novel time-domain clutter removal algorithm using high gain antennas for concealed object detections," *IEEE Transactions on Computational Imaging,* vol. 9, pp. 147-158, 2023.

[3] K. Kundu and N. N. Pathak, "Terahertz Technology and Its Importance in the Field of Biomedical Application: A Review," *Next Generation Wireless Communication: Advances in Optical, mm-Wave, and THz Technologies,* pp. 313-329, 2024.

[4] O. Yurduseven *et al.*, "Multibeam Si/GaAs holographic metasurface antenna at W-band," *IEEE Transactions on Antennas and Propagation,* vol. 69, no. 6, pp. 3523-3528, 2020.

[5] K. B. Cooper *et al.*, "G-band radar for humidity and cloud remote sensing," *IEEE Transactions on Geoscience and Remote Sensing,* vol. 59, no. 2, pp. 1106-1117, 2020.

[6] J. Zhang, R. Sharma, M. García-Fernández, G. Álvarez-Narciandi, M. A. B. Abbasi, and O. Yurduseven, "Deep Learning for Sensing Matrix Prediction in Computational Microwave Imaging With Coded-Apertures," *IEEE Access,* 2024.

[7] O. Yurduseven, D. L. Marks, T. Fromenteze, J. N. Gollub, and D. R. Smith, "Millimeter-wave spotlight imager using dynamic holographic metasurface antennas," *Optics Express,* vol. 25, no. 15, pp. 18230-18249, 2017.

[8] M. Boyarsky *et al.*, "Synthetic aperture radar with dynamic metasurface antennas: a conceptual development," *JOSA A,* vol. 34, no. 5, pp. A22-A36, 2017.

[9] T. Sleasman, "Dynamic metasurface apertures for computational imaging," Duke University, 2018.

[10] T. Fromenteze, O. Yurduseven, F. Berland, C. Decroze, D. R. Smith, and A. G. Yarovoy, "A transverse spectrum deconvolution technique for MIMO short-range Fourier imaging," *IEEE Transactions on Geoscience and Remote Sensing,* vol. 57, no. 9, pp. 6311-6324, 2019.

[11] A. M. Molaei, S. Hu, V. Skouroliakou, V. Fusco, X. Chen, and O. Yurduseven, "Fast processing approach for near-field terahertz imaging with linear sparse periodic array," *IEEE Sensors Journal,* vol. 22, no. 5, pp. 4410-4424, 2022.

[12] A. M. Molaei *et al.*, "Near-Field Bistatic Microwave Imaging with Dynamic Metasurface Antennas," in *2024 18th European Conference on Antennas and Propagation (EuCAP)*, 2024: IEEE, pp. 1-5.

[13] L. M. P. Mancera, "Analytical Modeling of Waveguide-fed Metasurfaces for Microwave Imaging and Beamforming," Duke University, 2018.

[14] L. Pulido-Mancera *et al.*, "Application of range migration algorithms to imaging with a dynamic metasurface antenna," *JOSA B,* vol. 33, no. 10, pp. 2082-2092, 2016.

[15] A. V. Diebold, L. Pulido-Mancera, T. Sleasman, M. Boyarsky, M. F. Imani, and D. R. Smith, "Generalized range migration algorithm for synthetic aperture radar image reconstruction of metasurface antenna measurements," *JOSA B,* vol. 34, no. 12, pp. 2610-2623, 2017.

[16] A. M. Molaei, V. Skouroliakou, V. Fusco, and O. Yurduseven, "Efficient 3D Image Reconstruction for Near-Field Microwave Imaging Using Dynamic Metasurface Antenna," *IEEE Access,* vol. 10, pp. 68491-68498, 2022.

[17] A. M. Molaei *et al.*, "Development of fast Fourier-compatible image reconstruction for 3D near-field bistatic microwave imaging with dynamic metasurface antennas," *IEEE Transactions on Vehicular Technology,* vol. 71, no. 12, pp. 13077-13090, 2022.

[18] G. Álvarez-Narciandi, M. García-Fernández, V. Skouroliakou, and O. Yurduseven, "Dynamic Metasurface Antenna-based Mills-Cross Aperture for 3D Computational Microwave Imaging," *IEEE Antennas and Wireless Propagation Letters,* 2024.

[19] O. Yurduseven, M. A. B. Abbasi, T. Fromenteze, and V. Fusco, "Frequency-diverse computational direction of arrival estimation technique," *Sci Rep,* vol. 9, no. 1, p. 16704, 2019.

[20] T. V. Hoang *et al.*, "Spatial diversity improvement in frequency-diverse computational imaging with a multi-port antenna," *Results in Physics,* vol. 22, p. 103906, 2021.

[21] O. Yurduseven, T. Fromenteze, C. Decroze, and V. F. Fusco, "Frequency-diverse computational automotive radar technique for debris detection," *IEEE Sensors Journal,* vol. 20, no. 22, pp. 13167-13177, 2020.

[22] A. M. Molaei *et al.*, "Application of Kirchhoff Migration Principle for Hardware-Efficient Near-Field Radar Imaging," *IEEE Transactions on Computational Imaging,* 2024.

[23] A. M. Molaei, T. Fromenteze, S. Hu, V. Fusco, and O. Yurduseven, "Fourier-based near-field three-dimensional image reconstruction in a multistatic imaging structure using dynamic metasurface antennas," *IEEE Transactions on Computational Imaging,* vol. 8, pp. 1089-1100, 2022.

[24] A. M. Molaei, P. del Hougne, V. Fusco, and O. Yurduseven, "Efficient joint estimation of DOA, range and reflectivity in near-field by using mixed-order statistics and a symmetric MIMO array," *IEEE Transactions on Vehicular Technology,* vol. 71, no. 3, pp. 2824-2842, 2021.

[25] V. Skouroliakou, A. M. Molaei, and O. Yurduseven, "Towards real-time three-dimensional (3d) imaging using dynamic metasurface antennas," in *2023 17th European Conference on Antennas and Propagation (EuCAP)*, 2023: IEEE, pp. 1-5.

[26] A. M. Molaei, V. Skouroliakou, V. Fusco, and O. Yurduseven, "Fourier-domain image reconstruction in near-field microwave imaging using a dynamic metasurface antenna: a sparse-sampling-based approach," in *Radar Sensor Technology XXVII*, 2023, vol. 12535: SPIE, pp. 239-249.

[27] S. Operto *et al.*, "Extending the search space of full-waveform inversion beyond the single-scattering Born approximation: A tutorial review," *Geophysics,* vol. 88, no. 6, pp. R671-R702, 2023.

[28] O. Yurduseven, V. R. Gowda, J. N. Gollub, and D. R. Smith, "Multistatic microwave imaging with arrays of planar cavities," *IET Microwaves, Antennas & Propagation,* vol. 10, no. 11, pp. 1174-1181, 2016.

[29] O. Yurduseven, J. N. Gollub, A. Rose, D. L. Marks, and D. R. Smith, "Design and simulation of a frequency-diverse aperture for imaging of human-scale targets," *IEEE access,* vol. 4, pp. 5436-5451, 2016.

[30] A. M. Molaei, B. Zakeri, and S. M. H. Andargoli, "Components separation algorithm for localization and classification of mixed near-field and far-field sources in multipath propagation," *IEEE Transactions on Signal Processing,* vol. 68, pp. 404-419, 2019.

[31] A. M. Molaei, S. Hu, R. Kumar, and O. Yurduseven, "Mimo coded generalized reduced dimension fourier algorithm for 3-d microwave imaging," *IEEE Transactions on Geoscience and Remote Sensing,* vol. 61, pp. 1-15, 2023.